Supporting Information for:

Nickel pyrophosphate combined with graphene nanoribbon used as efficient catalyst for OER

*Alan S. Souza,[a] Leticia S. Bezerra,[a] Eduardo S. F. Cardoso,[a] Guilherme V. Fortunato,[a,b] and Gilberto Maia[a,]**

[a] Institute of Chemistry, Federal University of Mato Grosso do Sul; Av. Senador Filinto Muller, 1555; Campo Grande, MS 79074–460, Brazil

[b] Institute of Chemistry of São Carlos, University of São Paulo, Avenida Trabalhador São-Carlense 400, São Carlos, SP 13566-590, Brazil

*Corresponding Author. E–mail: gilberto.maia@ufms.br

Tel.: +55 67 3345 3551. Fax: +55 67 3345 3552.

KOH electrolyte purification [1]

In a 50 mL polypropylene centrifuge tube previous cleaned with H_2SO_4 was added 2 g of $NiCl_2$ solubilized in 4 mL of ultrapure water followed by the addition of 1 M KOH to precipitate pure $Ni(OH)_2$, followed by shaken and centrifugation. The $Ni(OH)_2$ precipitated underwent six washing cycles with the addition to the tube of 20 mL of ultrapure water plus 2 mL of 1 M KOH, each cycle redispersing the $Ni(OH)_2$, centrifuging, and decanting the $Ni(OH)_2$. Finally was added 50 mL of 1 M KOH for purification in the polypropylene centrifuge tube containing only the cleaned $Ni(OH)_2$, redispersing by mechanical and sonication agitation for at least 30 min followed by rest at least for 3 hours, and finally centrifugation. The purified 1 M KOH supernatant was ready to use. [1]

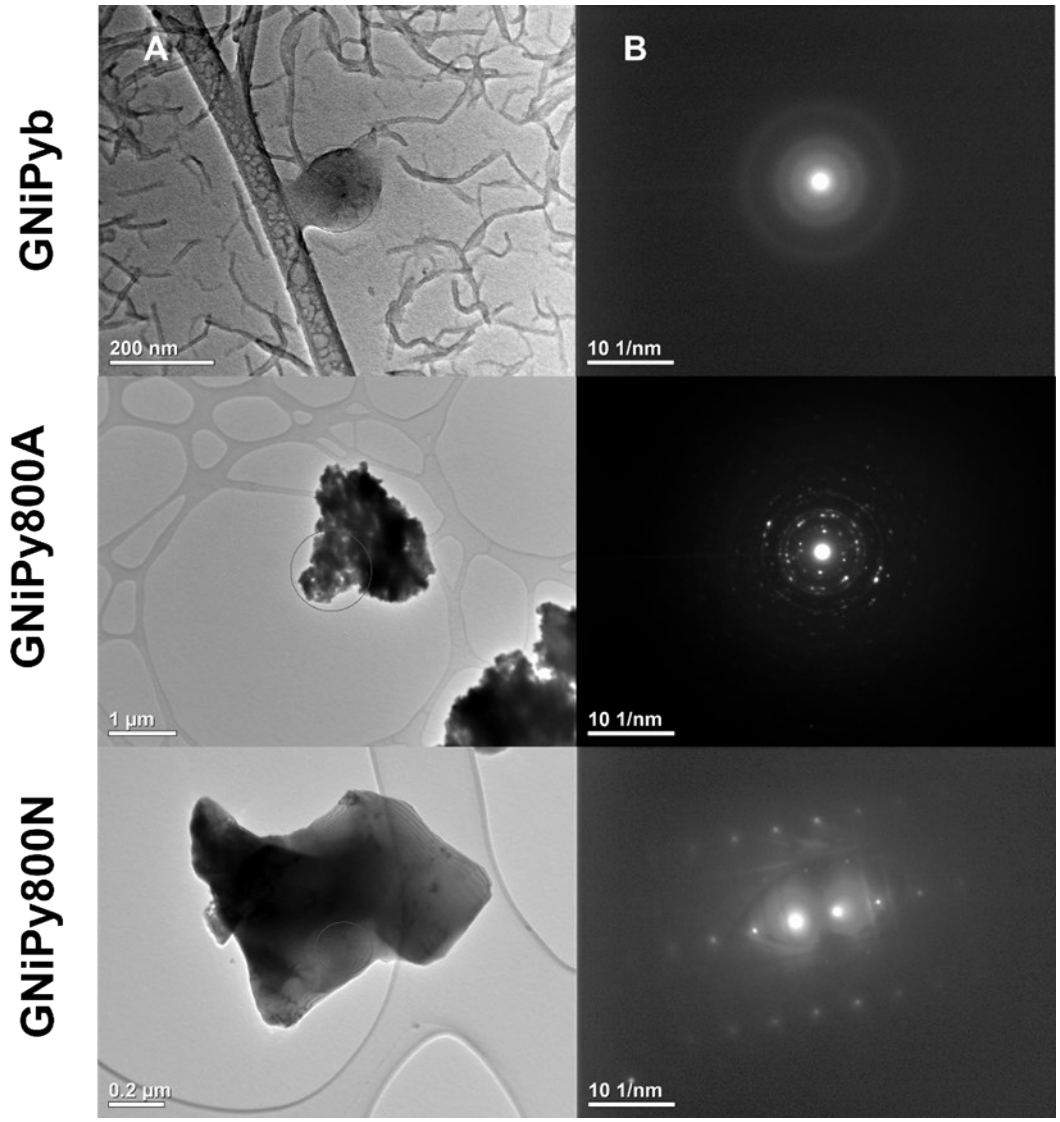

Figure S1. TEM images (A) and electron diffraction patterns (B) for the GNiPyb, GNiPy800A, and GNiPy800N nanocomposites.

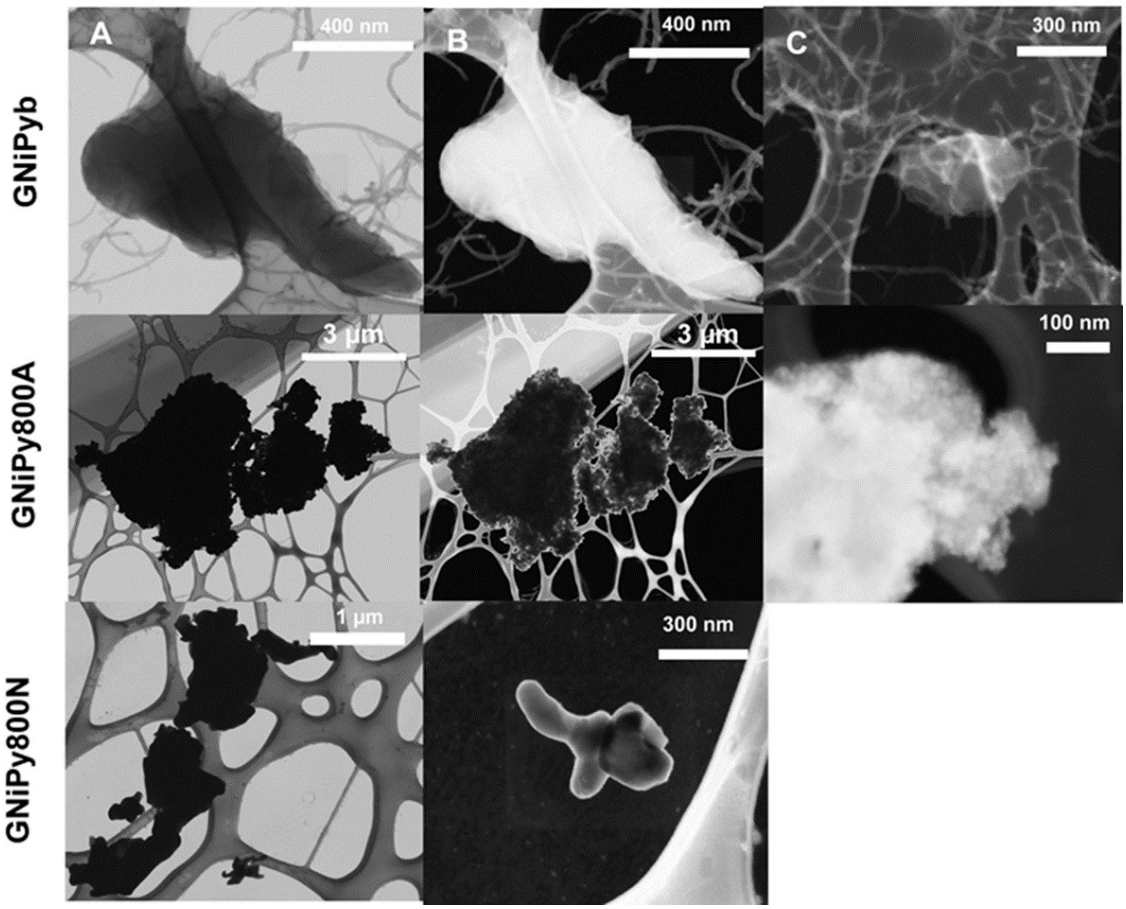

Figure S2. BF–STEM (A), DF–STEM (B), and HAADF–STEM (C) for the GNiPyb, GNiPy800A, and GNiPy800N nanocomposites.

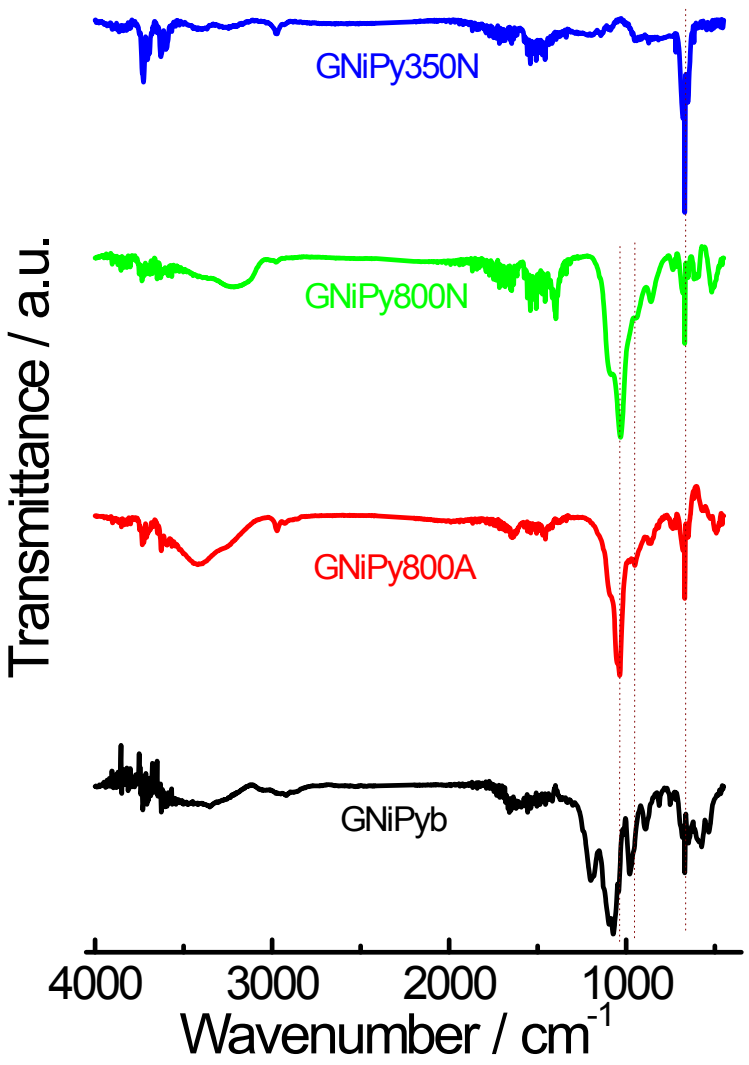

Figure S3. FT-IR spectra for the GNiPyb, GNiPy800A, GNiPy800N, and GNiPy350N nanocomposites.

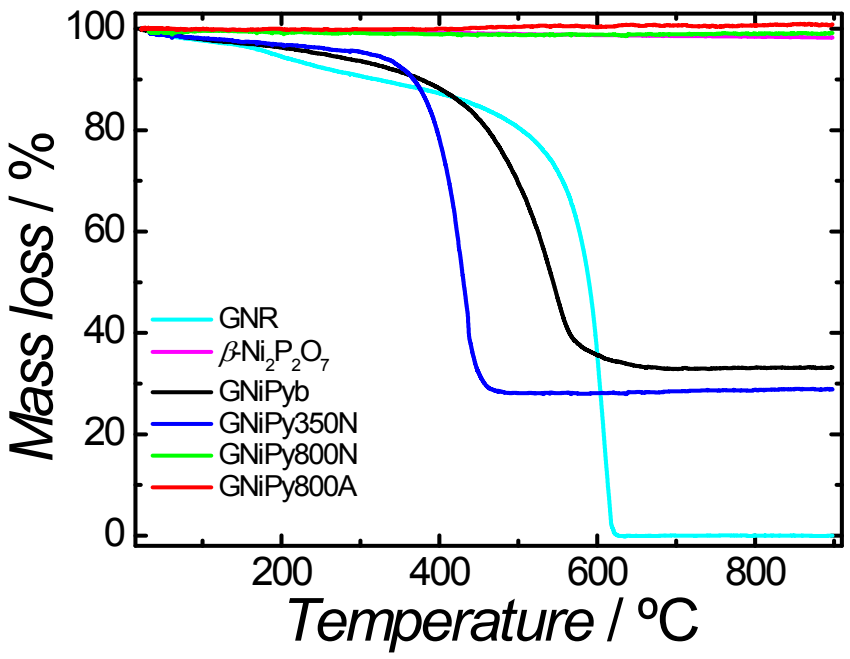

Figure S4. TG curves for the GNR, β-$Ni_2P_2O_7$, and GNiPyb, GNiPy350N, GNiPy800N, and GNiPy800A nanocomposites.

Table S1. EDX of mass composition and TG of unburned mass, and TG and EDX mass percentages of GNiPyb, GNiPy800A, GNiPy800N, and GNiPy350N nanocomposites.

Catalyst	EDX mass (%)	TG (mass unburned) (%)	TG and EDX mass (%)
GNiPyb	37.9 Ni 19.4 P - 42.7 O	33.1	12.6 Ni 6.4 P 66.9 C 14.1 O
GNiPy800A	65.4 Ni 0.5 P - 34.1 O	100	65.4 Ni 0.5 P 0 C 34.1 O
GNiPy800N	65.4 Ni 4.7 P - 29.9 O	100	65.4 Ni 4.7 P 0 C 29.9 O
GNiPy350N	64.7 Ni 0.5 P - 34.8 O	29.6	19.2 Ni 0.1 P 70.4 C 10.3 O

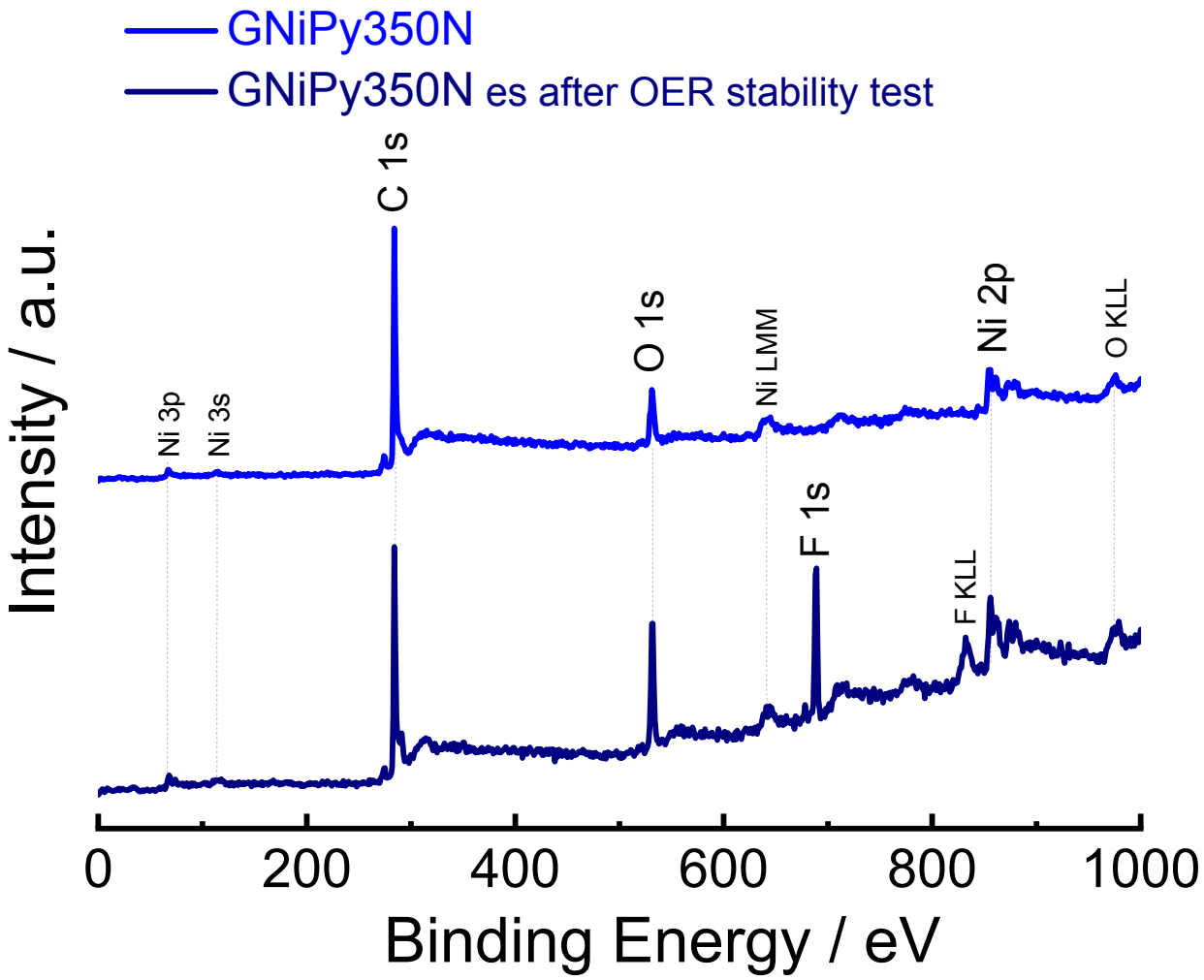

Figure S5. XPS survey spectra of the GNiPy350N nanocomposites.

Table S2. Positions, relative sensitive factors (R.S.F.), atomic and mass percentages obtained from the XPS spectra shown in Figure S5 for the GNiPy350N nanocomposites.

Catalyst	Name	Position (eV)	R.S.F.	Content (at. %)	Content (mass %)
GNiPy350N	O 1s	531	2.93	10.25	11.88
	C 1s	284	1	86.79	75.52
	Ni 2p	854	22.2	2.96	12.6

Table S3. Positions, relative sensitive factors (R.S.F.), atomic and mass percentages obtained from the XPS spectra shown in Figure S5 for the es GNiPy350N nanocomposites.

Catalyst	Name	Position (eV)	R.S.F.	Content (at.%)	Content (mass %)
GNiPy350N	O 1s	531	2.93	18.28	19.69
	C 1s	284	1	77.19	62.41
	Ni 2p	856	22.2	4.53	17.9

Table S4. Positions and percentages of content of functional groups or chemical states present in the GNiPy350N nanocomposite obtained from high–resolution XPS spectra shown in Figure 5.

Catalyst	Name	Chemical state	Position (eV)	% content
GNiPy350N	P 2p	P $2p_{3/2}$	132.85	61.24
		P $2p_{1/2}$	133.78	38.76
	O 1s	Ni–O	529.07	23.65
		P–O	530.57	29.22
		C=O	531.46	20.68
		C–O	532.66	19.59
		H_2O	533.84	6.86
	C 1s	C=C	283.95	77.81
		C–C	285.25	16.03
		C–OH & C–O	286.59	4.8
		C=O & COOH	288.41	1.36
	Ni 2p	Ni $2p_{3/2}$	854.69	32.85
		satellite	860.71	35.05
		Ni $2p_{1/2}$	872.37	14.53
		satellite	878.78	17.58

Table S5. Positions and percentages of content of functional groups or chemical states present in the es GNiPy350N nanocomposite obtained from high–resolution XPS spectra shown in Figure 5.

Catalyst	Name	Chemical state	Position (eV)	% content
GNiPy350N	P 2p	P $2p_{3/2}$	133.72	60.81
		P $2p_{1/2}$	135.10	39.19
	C 1s	C=C	283.96	73.42
		C–C	284.97	19.72
		C–OH & C–O	286.4	4.3
		C=O & COOH	288.17	2.56
	O 1s	Ni–O	529.14	4.07
		P–O	530.76	30.04
		C=O	531.46	41.81
		C–O	532.65	16.63
		H_2O	533.85	7.46
	Ni 2p	Ni $2p_{3/2}$	855.87	31.94
		satellite	861.61	31.9
		Ni $2p_{1/2}$	873.45	14.35
		satellite	879.86	21.81

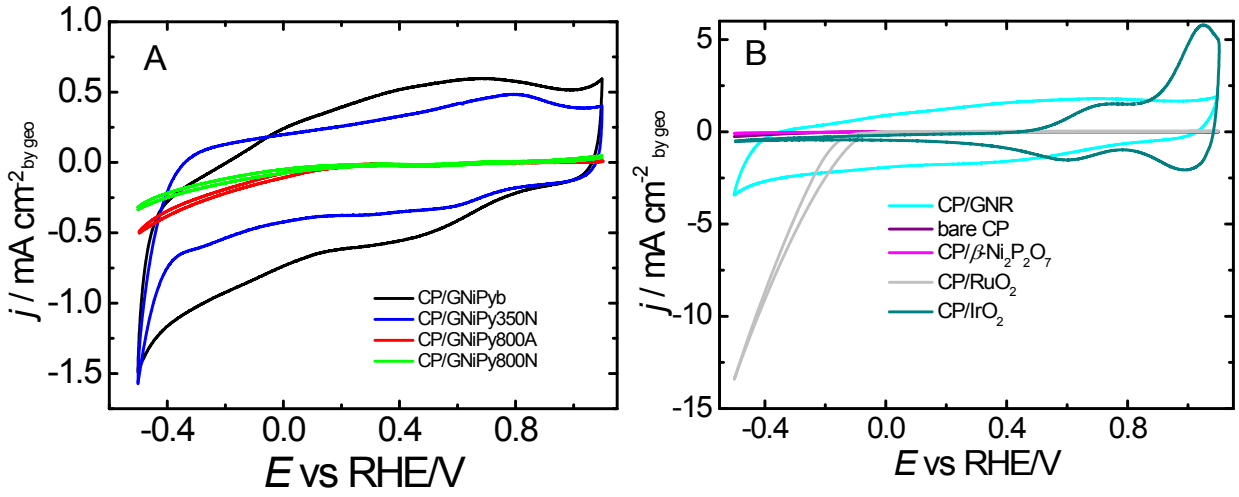

Figure S6. Cyclic voltammograms for bare and modified CP electrodes in N_2–saturated 1 M KOH solution. Potential scan rate: 50 mV s^{-1}. Scans were initiated at 1.1 V. The surfaces of the GNiPy350N and CP/IrO_2 electrodes were covered with 15 µL of 0.1% Nafion solution.

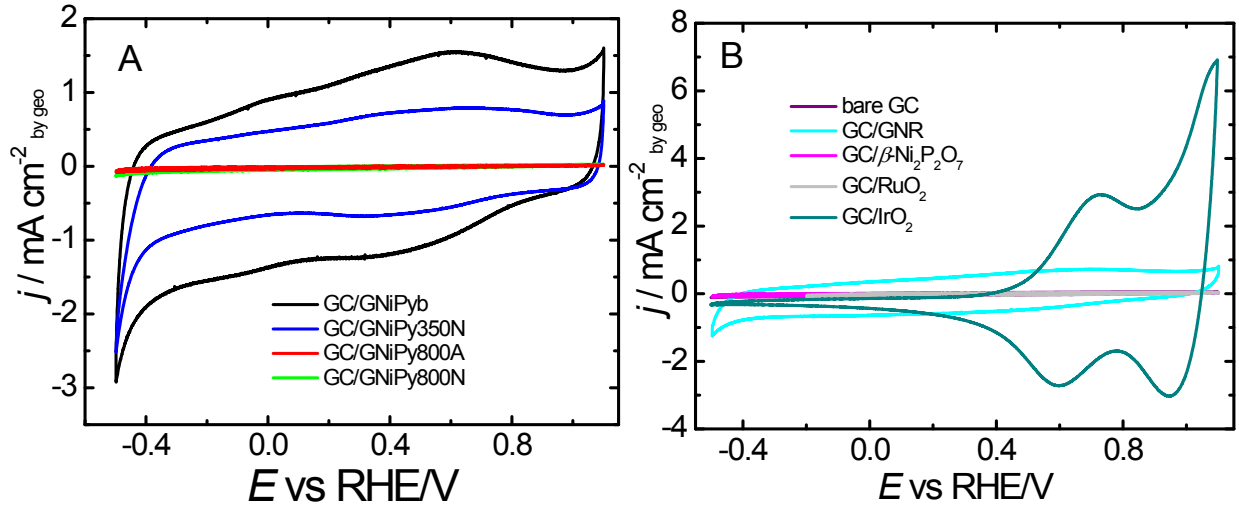

Figure S7. Cyclic voltammograms for bare and modified GC electrodes in N_2–saturated 1 M KOH solution. Potential scan rate: 50 mV s^{-1}. Scans were initiated at 1.1 V. The surfaces of the GC/GNiPy350 and GC/IrO_2 electrodes were covered with 5 µL of 0.1% Nafion solution.

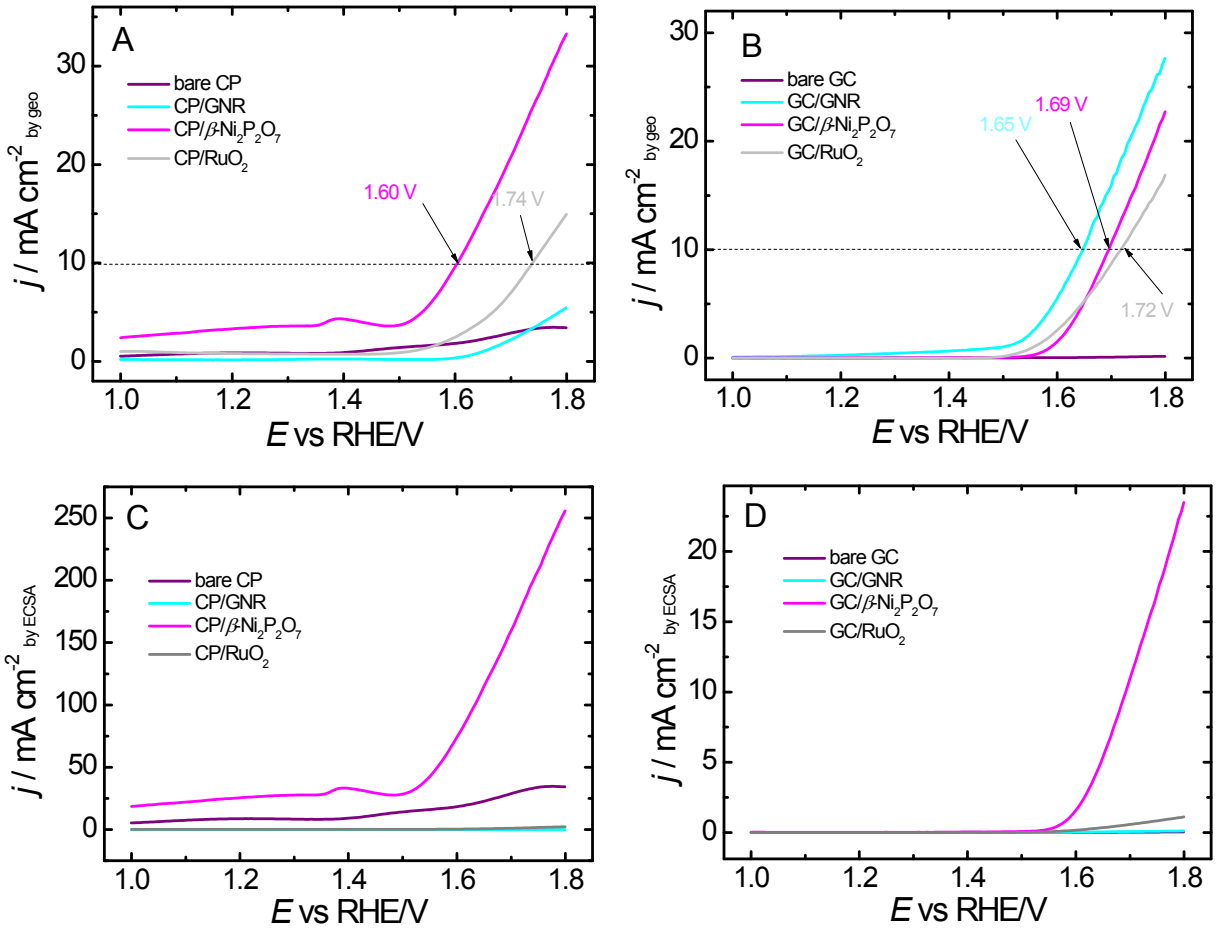

Figure S8. Stationary linear voltammograms recorded for bare and modified CP (A and C) and hydrodynamic linear voltammograms recorded for bare and modified GC electrodes (B and D) in O_2–saturated 1 M KOH solution, with $\nu = 5$ mVs^{-1}. Scans were initiated at 1.0 V.

Table S6. Values related to overpotential at current density of 10 mA cm^{-2} (η_j at 10 mA cm^{-2} from Figures 6A and S8A), Tafel slopes (Figure S9), double layer capacitance (C_{dl}) (obtained from Figures S15, S17, and S19), and electrochemically active surface area (ECSA) (obtained from Figures S16, S18, and S20) obtained for bare and modified CP electrodes. Catalysts loading = 150 μg cm^{-2}.

Electrode	η_j at 10 mA cm^{-2} (V)	Tafel slope (mV dec^{-1})	R_{ct} (Ω)			C_{dl} (μF)			ECSA (cm^2)		
			Initial	After OER	After OER stability	Initial	After OER	After OER stability	Initial	After OER	After OER stability
CP/IrO_2	0.30	59	1.7	148	high	16000	1660	408	400	41.5	2.7
CP/GNiPy350N	0.32	136	1.7	6.6	4.3	1270	1320	608	31.8	33	15.2
CP/GNiPyb	0.37	150	0.7	42	high	3170	390	245	79.3	9.75	6.1
CP/β-$Ni_2P_2O_7$	0.37	205	very high	1140	–	5.1	3.51	-	0.13	0.09	-
CP/GNiPy800A	0.39	168	very high	very high	high	3.0	6.8	97.9	0.07	0.17	0.23
CP/GNiPy800N	0.41	133	17.6	very high	359	5.6	32	7.07	0.14	0.80	0.19
CP/RuO_2	0.51	207	5.7	32.5	–	265	3.92	–	6.62	0.10	–
CP/GNR	–	112	0.7	high	–	8550	3910	–	214	97.7	–
bare CP	–	474	very high	very high	–	3.92	3.92	–	0.10	0.10	–

Table S7. Values related to overpotential at current density of 10 mA cm^{-2} (η_j at 10 mA cm^{-2} from Figures 6B and S8B), Tafel slopes (Figure S10), double layer capacitance (C_{dl}) (obtained from Figures S21 and S23), and electrochemically active surface area (ECSA) (obtained from Figures S22 and S24) obtained for bare and modified GC electrodes. Catalysts loading = 150 μg cm^{-2}.

Electrode	η_j at 10 mA cm^{-2} (V)	Tafel slope (mV dec^{-1})	R_{ct} (Ω)		C_{dl} (μF)		ECSA (cm^2)	
			Initial	After OER	Initial	After OER	Initial	After OER
GC/IrO_2	0.25	52.2	1.8	2.5	4420	1560	111	39.0
GC/GNiPy350N	0.34	50.7	3.3	7.8	1320	175	33.0	4.40
GC/GNiPyb	0.42	74.9	0.7	3.6	581	123	14.5	3.10
GC/β-$Ni_2P_2O_7$	0.46	80.1	very high	high	7.73	10	0.19	0.25
GC/GNiPy800A	0.38	74.1	very high	very high	8.08	9.55	0.20	0.24
GC/GNiPy800N	0.46	128	very high	very high	20	18.1	0.50	0.45
GC/RuO_2	0.46	124	11.7	1.2	119	123	2.97	3.10
GC/GNR	0.42	115	6.6	high	1850	2.46	46.2	6.15
bare GC	–	339	very high	high	29.6	25.8	0.74	0.64

Table S8. Summary of results related to OER activity obtained for the pyrophosphates investigated in the present study and the results reported by studies published in the literature.

Catalyst	Loading ($\mu g\ cm^{-2}$)	η_j at 10 $mA\ cm^{-2}$ (V)	Tafel slope ($mV\ dec^{-1}$)	Solution	Synthesis method	Ref.
β-$Ni_2P_2O_7$/GNR - 350 ºC	150	0.32	68	1.0 M KOH	Calcination	**Present study**
NFPy	255	0.29 upon GC surface	47.4	1.0 M KOH	Stirring	[2]
$Na_2Ni_{0.75}Fe_{0.25}P_2O_7$-nano	1,000	0.30	110	0.1 M KOH	Annealed	[3]
Ni–Co-hydroxide/$Ni_2P_2O_7$ nano-micro-structured	Not reported	0.20 upon Ni foam	76	1.0 M KOH	Hydrothermal and electrodeposition	[4]
Fe-Ni_2P@N,PCNSs	127	0.39	96	0.1 M KOH	Calcination	[5]
$Ni_2P_2O_7$ microsheets	1,500	0.21 upon highly porous surface	64.1	1.0 M KOH	Thermal treatment	[6]
$Ni_2P_2O_7 \cdot 8H_2O$	Not reported	0.24 upon stainless steel	51.5	1.0 M KOH	Chemical bath deposition	[7]
$Na_2CoP_2O_7$/rGO (50/50 wt%)	1,717	0.24	63	1.0 M KOH	Annealing	[8]
$Co_2P_2O_7$	Not reported	0.27	59.8	1.0 M KOH	Hydrothermal	[9]
NCFPO/C NPs	1,000	0.30	47	0.1 M KOH and 0.5 M NaCl + 0.1 M KOH	Sol−gel process followed by heat treatment	[10]
$Co_2P_2O_7$@N,P-C	500	0.27	49.1	1.0 M	Pyrolysis	[11]

				KOH		
NMPy	140	0.47	64	0.1 M KOH	Mechanochemical assisted solid-state synthesis and annealing	[12]
CoPi/NPGA	200	0.34	96	1.0 M KOH	Hydrothermal process and subsequent pyrolysis strategy	[13]
CoPPi nanowires	500	0.36	54.1	1.0 M KOH	Low-temperature hydrothermal method	[14]
CoHPi	200	0.31	31	1.0 M KOH	Chemical conversion of α-$Co(OH)_2$ precursor at room temperature	[15]
CoNiPP-600	510	0.26	60	1.0 M KOH	Hydrothermal method followed by annealing	[16]
Co-Fe-Pyro	570	0.28	32	1.0 M KOH	Co-precipitation method	[17]

NFPy = porous iron-doped nickel pyrophosphate; Fe-Ni_2P@N,PCNSs = Fe-Ni_2P particles supported on N,P-codoped porous carbon nanosheets; $Na_2CoP_2O_7$/rGO (50/50 wt%) = hollow spherical powder possessing nano-thick walls of sodium-cobalt pyrophosphate and reduced graphene oxide; $Co_2P_2O_7$ = cobalt pyrophosphate nanosheets; NCFPO/C NPs = carbon-coated sodium cobalt−iron pyrophosphate ($Na_2Co_{1-x}Fe_xP_2O_7$/C, $0 \leq x \leq 1$) nanoparticles; $Co_2P_2O_7$@N,P-C = $Co_2P_2O_7$@N, P co-doped carbon nanocages; NMPy = $Na_2MnP_2O_7$ pyrophosphate; CoPi/NPGA = N,P-codoped three-dimensional (3D) reduced graphene-oxide-aerogel-supported (rGOA-supported) $Co_2P_2O_7$ (CoPi) fine particles; CoPPi = cobalt pyrophosphate nanostructures; CoHPi = two-dimensional cobalt hydrogen phosphate; CoNiPP-600 = $CoNiP_2O_7$ at T= 600 °C; Co-Fe-Pyro = cobalt iron pyrophosphate.

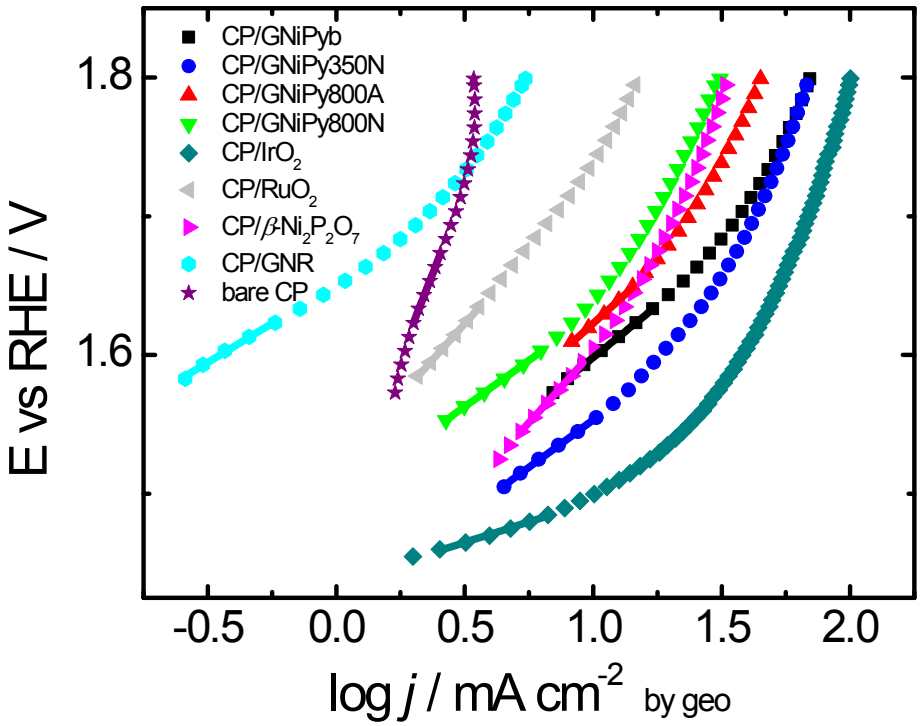

Figure S9. Tafel plots based on data (in OER) from Figures 6A and S8A for modified CP electrodes in O_2–saturated 1.0 M KOH solution.

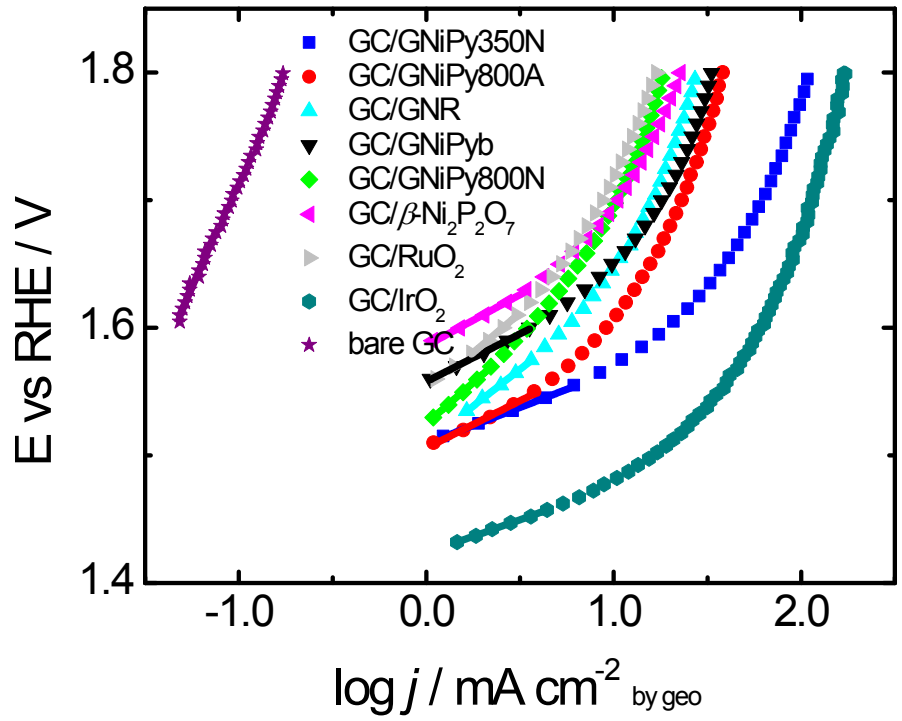

Figure S10. Tafel plots based on data (in OER) from Figures 6B and S8B for modified GC electrodes in O_2–saturated 1.0 M KOH solution.

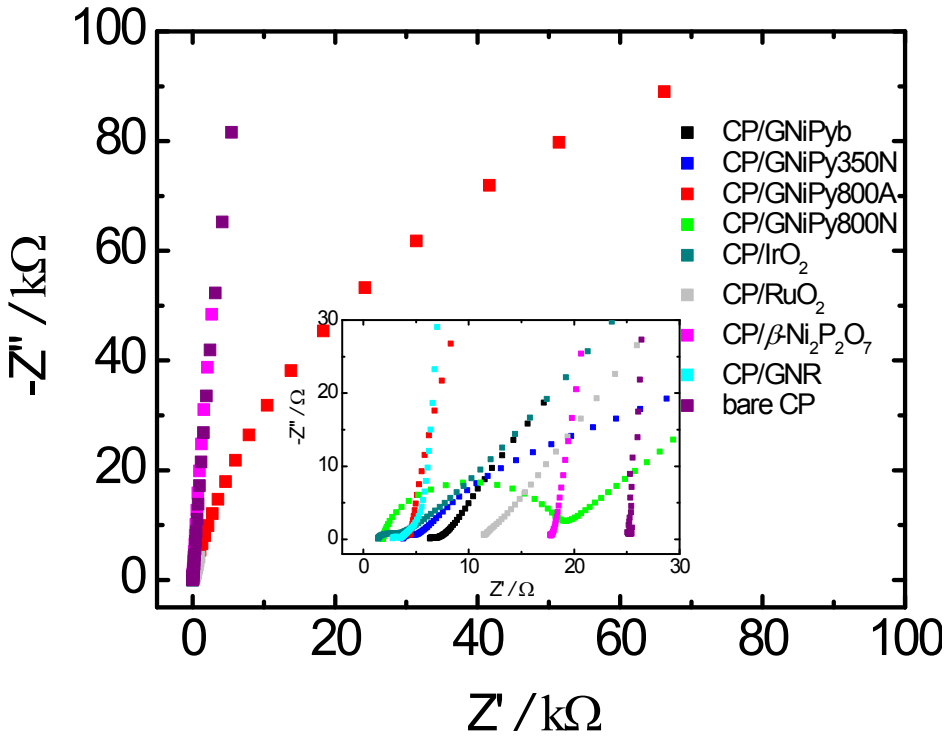

Figure S11. EIS results for bare and modified CP electrodes in N_2–saturated 1 M KOH solution, before OER. Potential perturbation: 10mV (rms). Frequency range: 100kHz – 10 mHz. Constant potential for EIS acquisition: OCP (0.83 V vs. RHE on average).

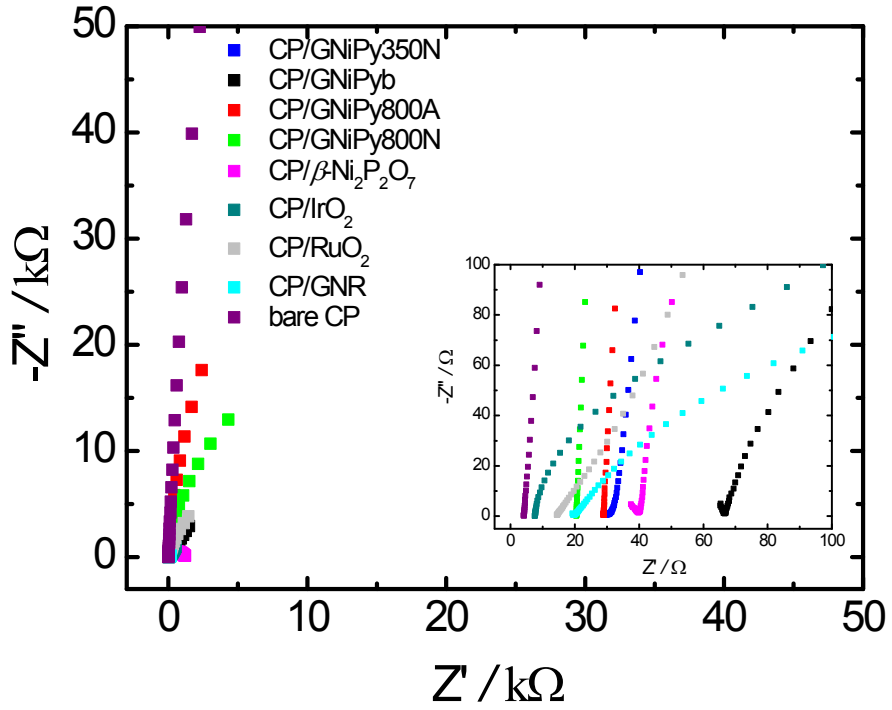

Figure S12. EIS results for bare and modified CP electrodes in N_2–saturated 1 M KOH solution after 3 consecutive OER analyses. Potential perturbation: 10mV (rms). Frequency range: 100kHz – 10 mHz. Constant potential for EIS acquisition: OCP (0.85 V vs. RHE on average).

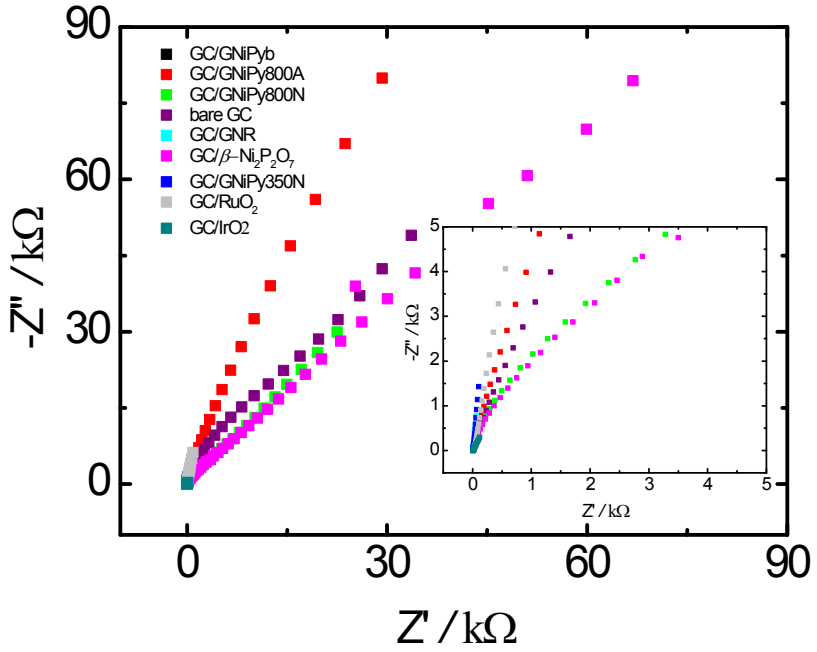

Figure S13. EIS results for bare and modified GC electrodes in N_2–saturated 1 M KOH solution, before OER. Potential perturbation: 10mV (rms). Frequency range: 100kHz – 10 mHz. Constant potential for EIS acquisition: OCP (0.88 V vs. RHE on average).

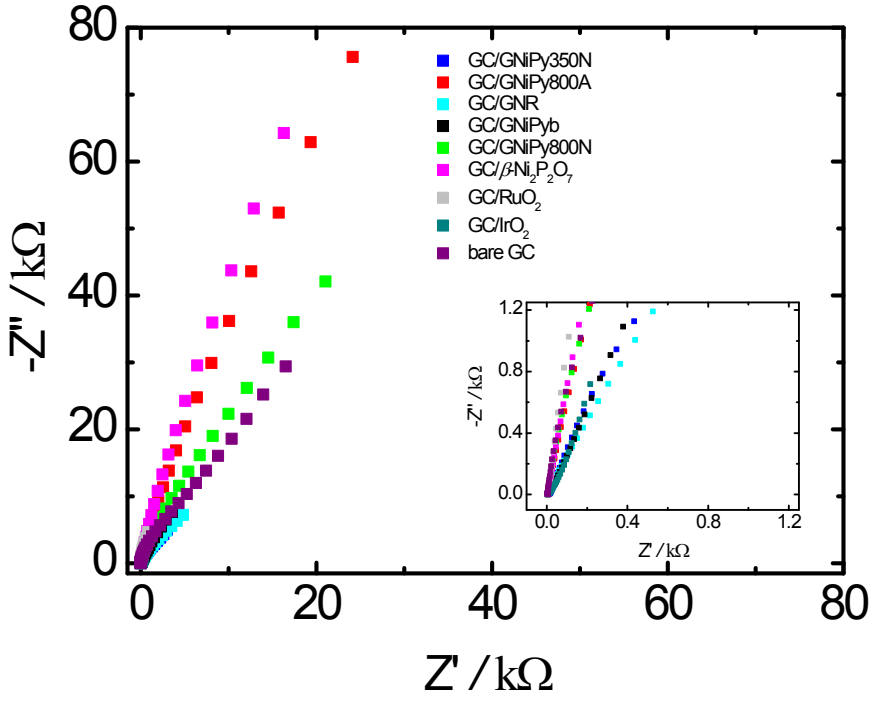

Figure S14. EIS results for bare and modified GC electrodes in N_2–saturated 1 M KOH solution after 3 consecutive OER analyses. Potential perturbation: 10mV (rms). Frequency range: 100kHz – 10 mHz. Constant potential for EIS acquisition: OCP (0.86 V vs. RHE on average).

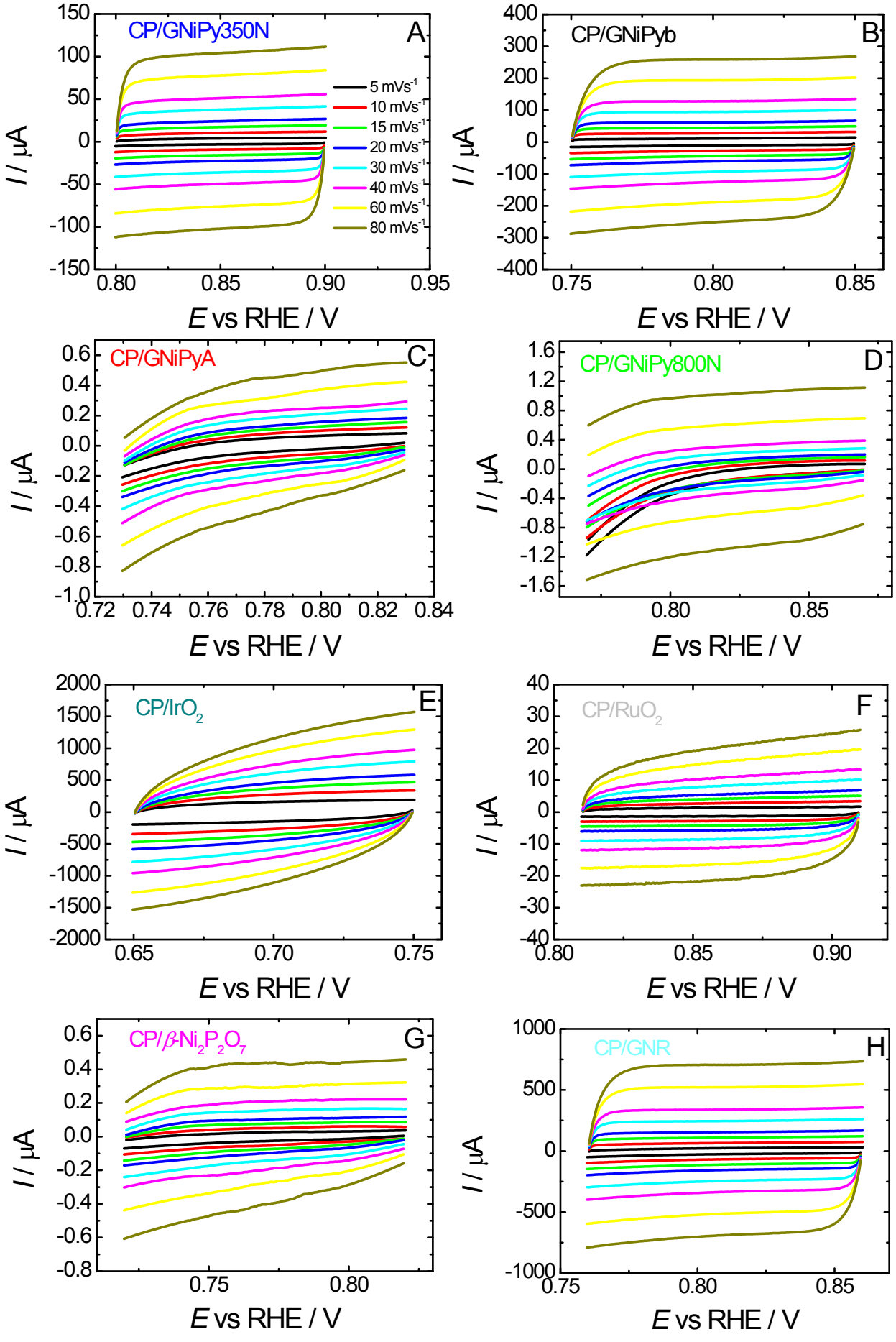
CP/GNiPy350N
A
5 mVs-1
10 mVs-1
15 mVs-1
20 mVs-1
30 mVs-1
40 mVs-1
60 mVs-1
80 mVs-1
I / μA
E vs RHE / V
CP/GNiPyb
B
CP/GNiPyA
C
CP/GNiPy800N
D
CP/IrO2
E
CP/RuO2
F
CP/β-Ni2P2O7
G
CP/GNR
H

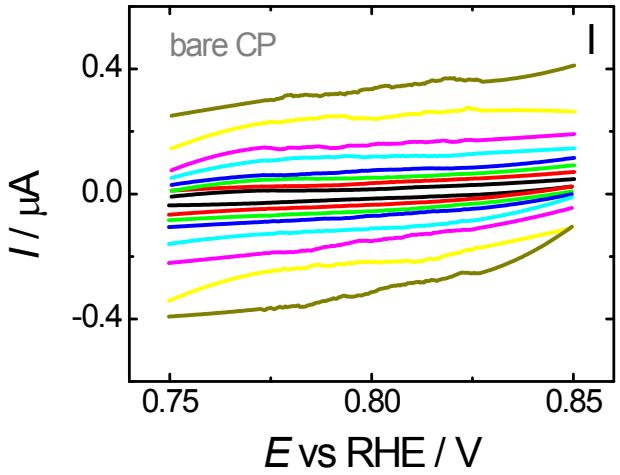

Figure S15. Cyclic voltammograms obtained in a non–Faradaic potential region – which also consisted of the open circuit potential (OCP) – for modified CP electrodes in N_2–saturated 1M KOH solution, before OER. The modified electrodes were kept in each vertex potential for 10 sec before the beginning of the next potential sweep. Scans were initiated at higher potentials.

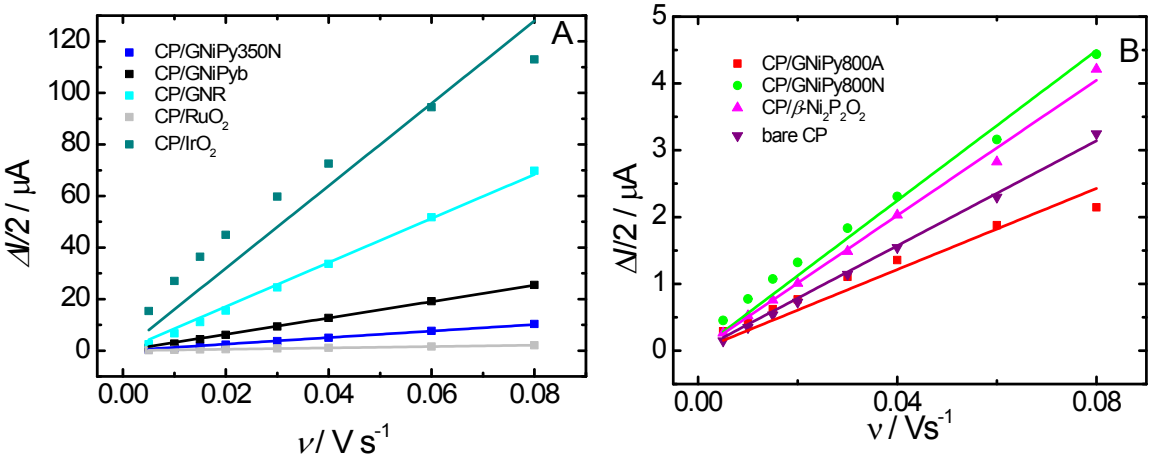

Figure S16. Plots related to differences between the anodic and the cathodic double layer charging currents (Figure S15, before OER) divided by 2 (($\Delta I = I_a - I_c$)/2), measured at the OCP, which is also in a non–Faradaic potential region, relative to the potential scan rates. The slopes of these plots yield the double–layer capacitance (C_{dl}) values (see Table S6) used for determining the ECSA for the modified CP electrodes in N_2–saturated 1 M KOH solution.

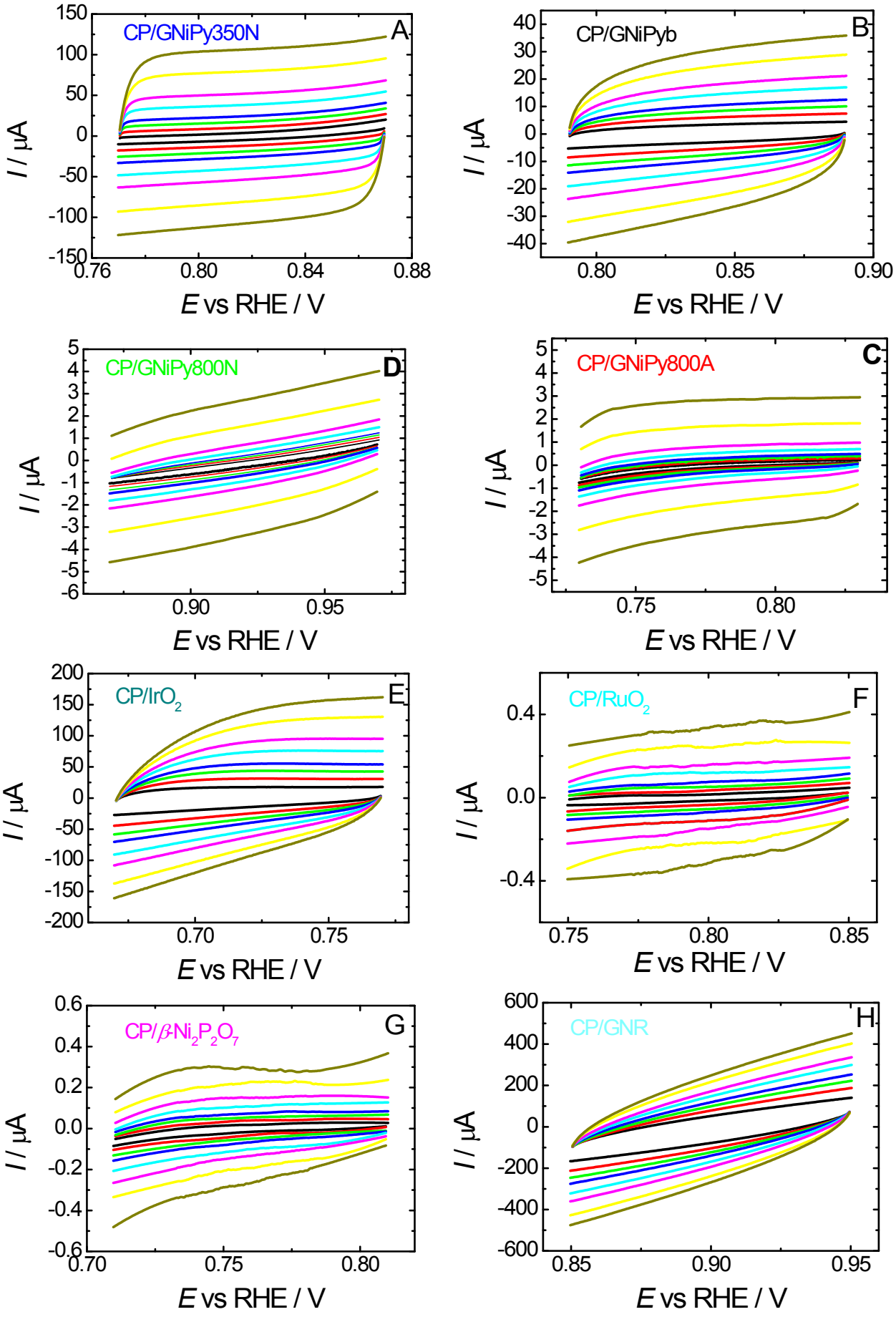
CP/GNiPy350N
A
I / μA
E vs RHE / V
CP/GNiPyb
B
CP/GNiPy800N
D
CP/GNiPy800A
C
CP/IrO2
E
CP/RuO2
F
CP/β-Ni2P2O7
G
CP/GNR
H

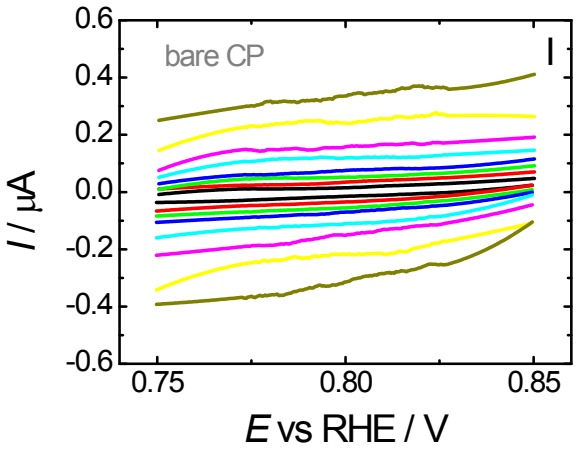

Figure S17. Cyclic voltammograms measured in a non–Faradaic potential region – which also consisted of the open circuit potential (OCP) – for modified CP electrodes in N_2–saturated 1M KOH solution, after OER. The modified electrodes were kept in each vertex potential for 10 sec before the onset of the next potential sweep. Scans were initiated at higher potentials.

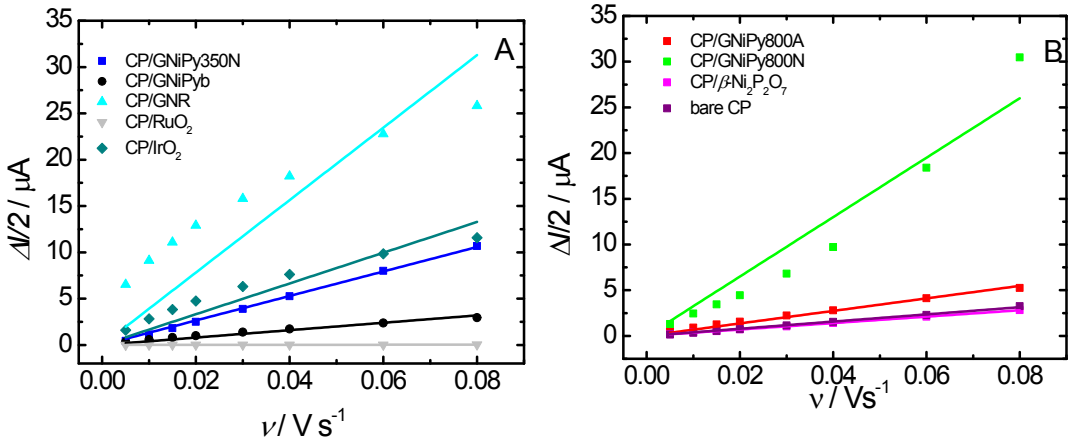

Figure S18. Plots related to differences between the anodic and the cathodic double layer charging currents (Figure S17, after OER) divided by 2 (($\Delta I = I_a – I_c$)/2), measured at the OCP, which is also in a non–Faradaic potential region, relative to the potential scan rates. The slopes of these plots yield the double–layer capacitance (C_{dl}) values (see Table S6) used for determining the ECSA for the modified CP electrodes in N_2–saturated 1 M KOH solution.

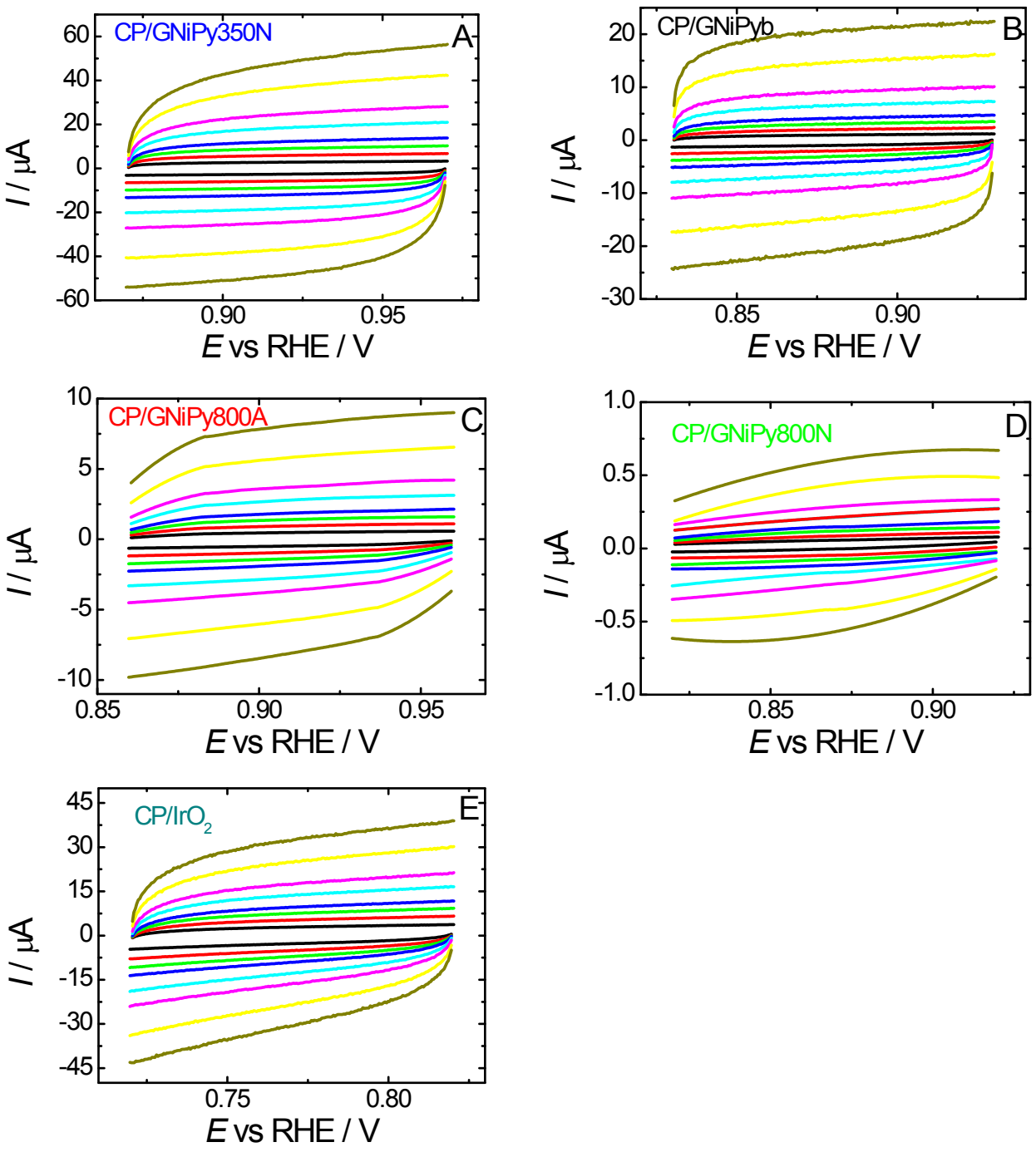

Figure S19. Cyclic voltammograms measured in a non–Faradaic potential region – which also consists of the open circuit potential (OCP) – for modified CP electrodes in N_2–saturated 1M KOH solution after OER stability test. The modified electrodes were kept in each vertex potential for 10 sec before the onset of the next potential sweep. Scans were initiated at higher potentials.

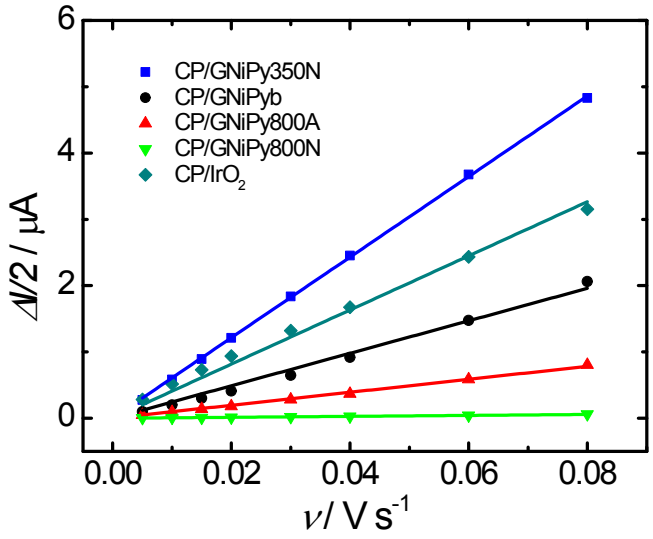

Figure S20. Plots related to differences between the anodic and the cathodic double layer charging currents (Figure S19, after OER stability test) divided by 2 (($\Delta I = I_a – I_c$)/2), measured at the OCP, which is also in a non–Faradaic potential region, relative to the potential scan rates. The slopes of these plots yield the double–layer capacitance (C_{dl}) values (see Table S6) used for determining the ECSA for the modified CP electrodes in N_2–saturated 1 M KOH solution.

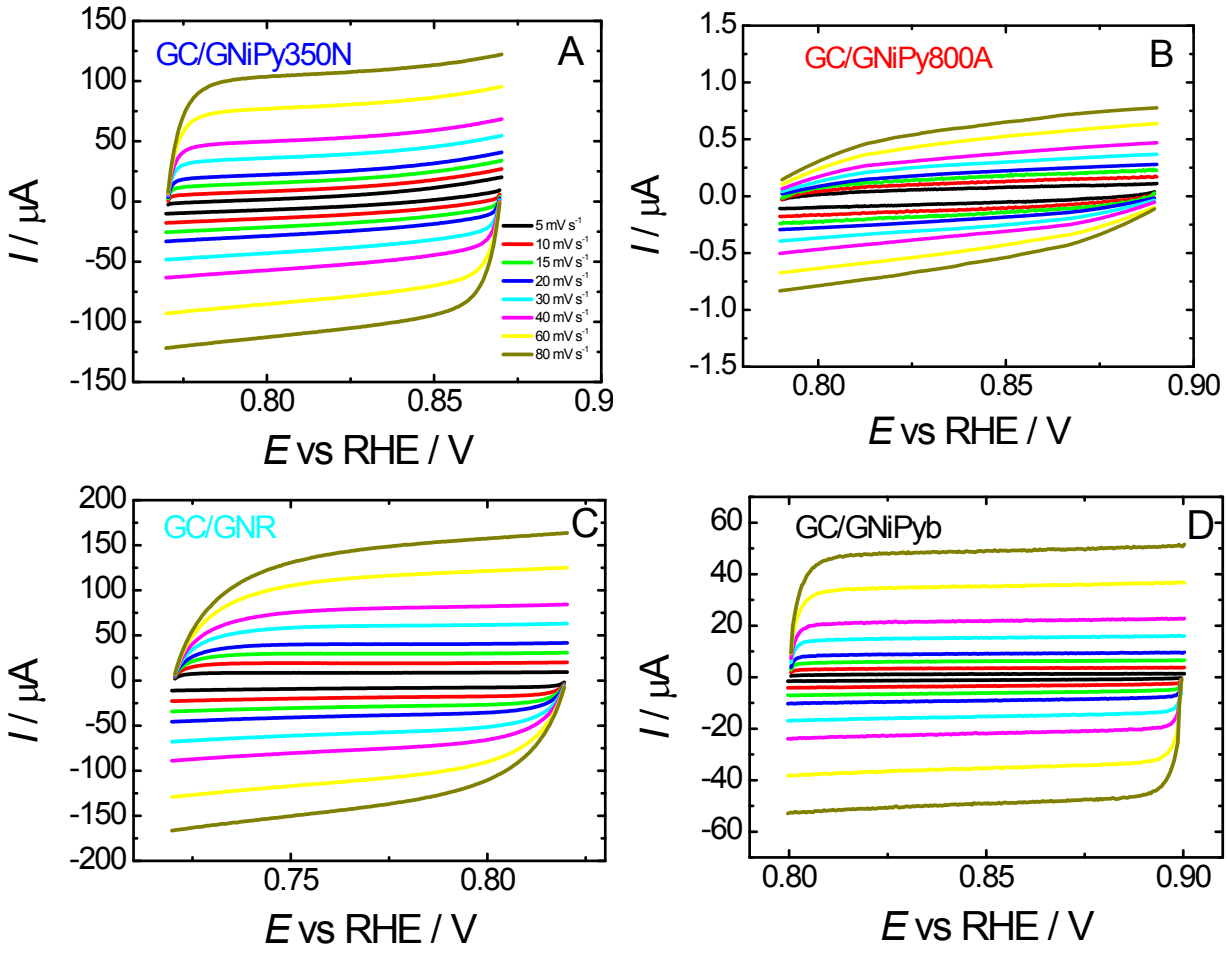
GC/GNiPy350N
A
GC/GNiPy800A
B
GC/GNR
C
GC/GNiPyb
D
I / μA
E vs RHE / V
5 mV s-1
10 mV s-1
15 mV s-1
20 mV s-1
30 mV s-1
40 mV s-1
60 mV s-1
80 mV s-1

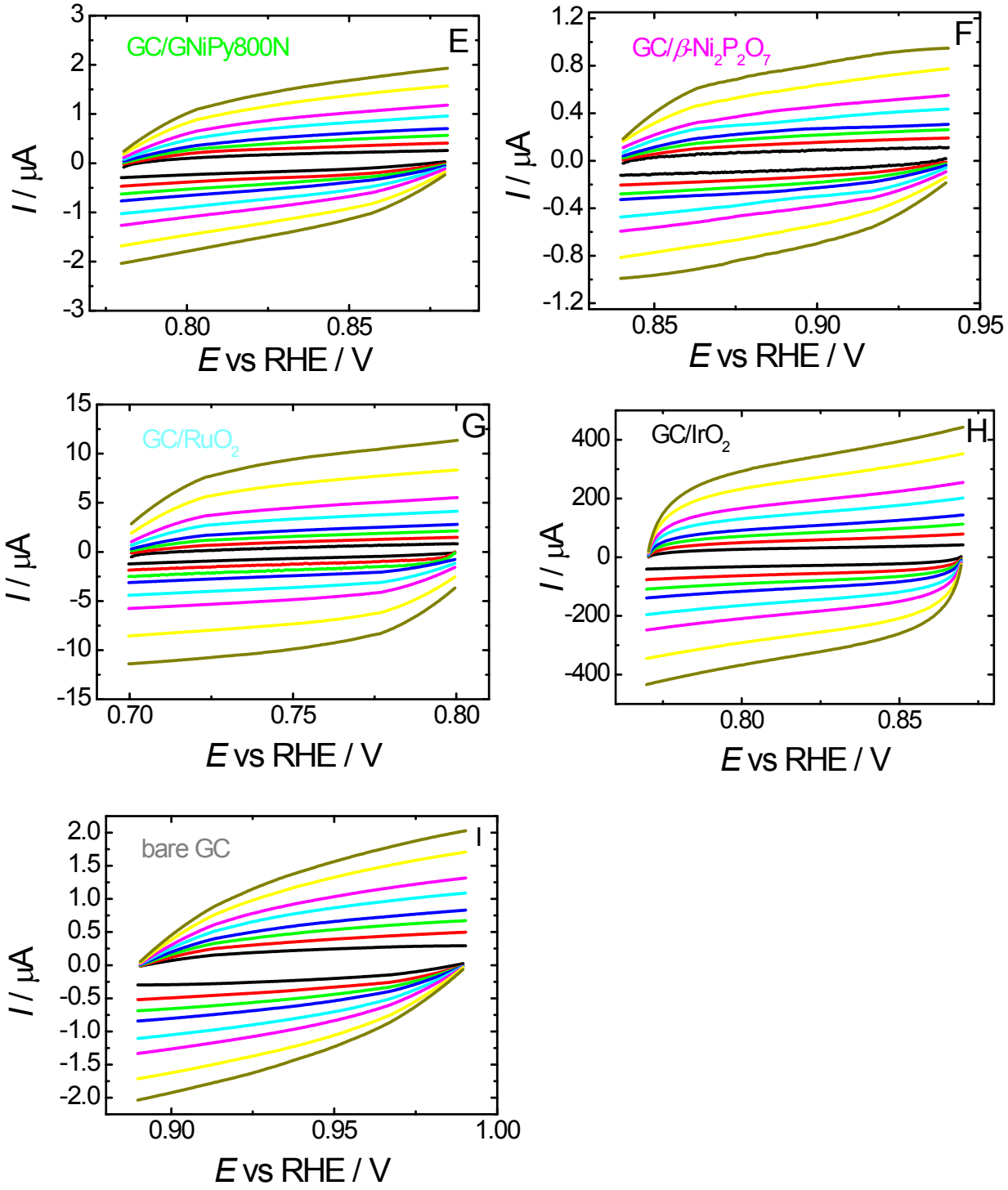

Figure S21. Cyclic voltammograms measured in a non–Faradaic potential region – which also consists of the open circuit potential (OCP) – for modified GC electrodes in N_2–saturated 1M KOH solution before OER. The modified electrodes were kept in each vertex potential for 10 sec before the onset of the next potential sweep. Scans were initiated at higher potentials.

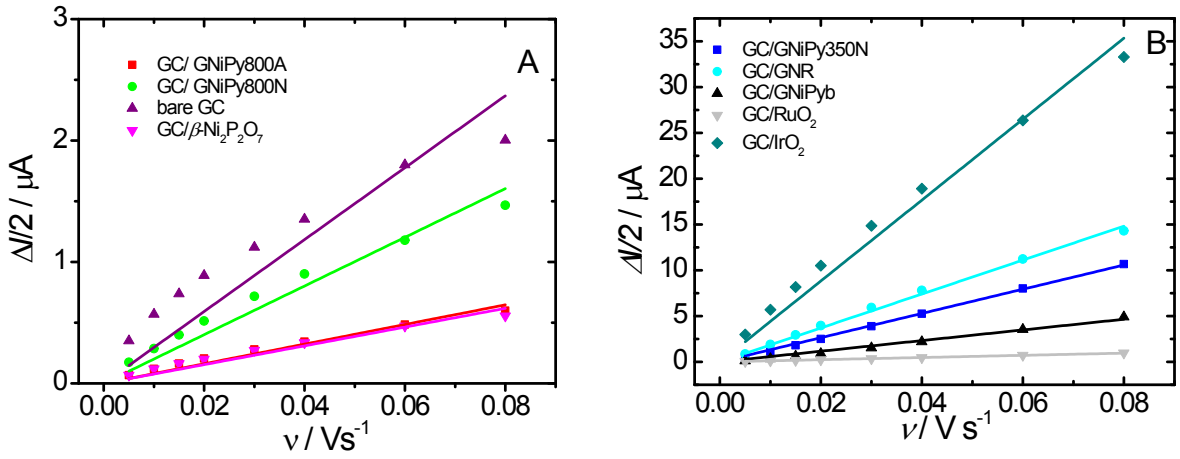

Figure S22. Plots related to differences between the anodic and the cathodic double layer charging currents (Figure S21, before OER) divided by 2 (($\Delta I = I_a – I_c$)/2), measured at the OCP, which is also in a non–Faradaic potential region, relative to the potential scan rates. The slopes of these plots yield the double–layer capacitance (C_{dl}) values (see Table S7) used for determining the ECSA for the modified GC electrodes in N_2–saturated 1 M KOH solution.

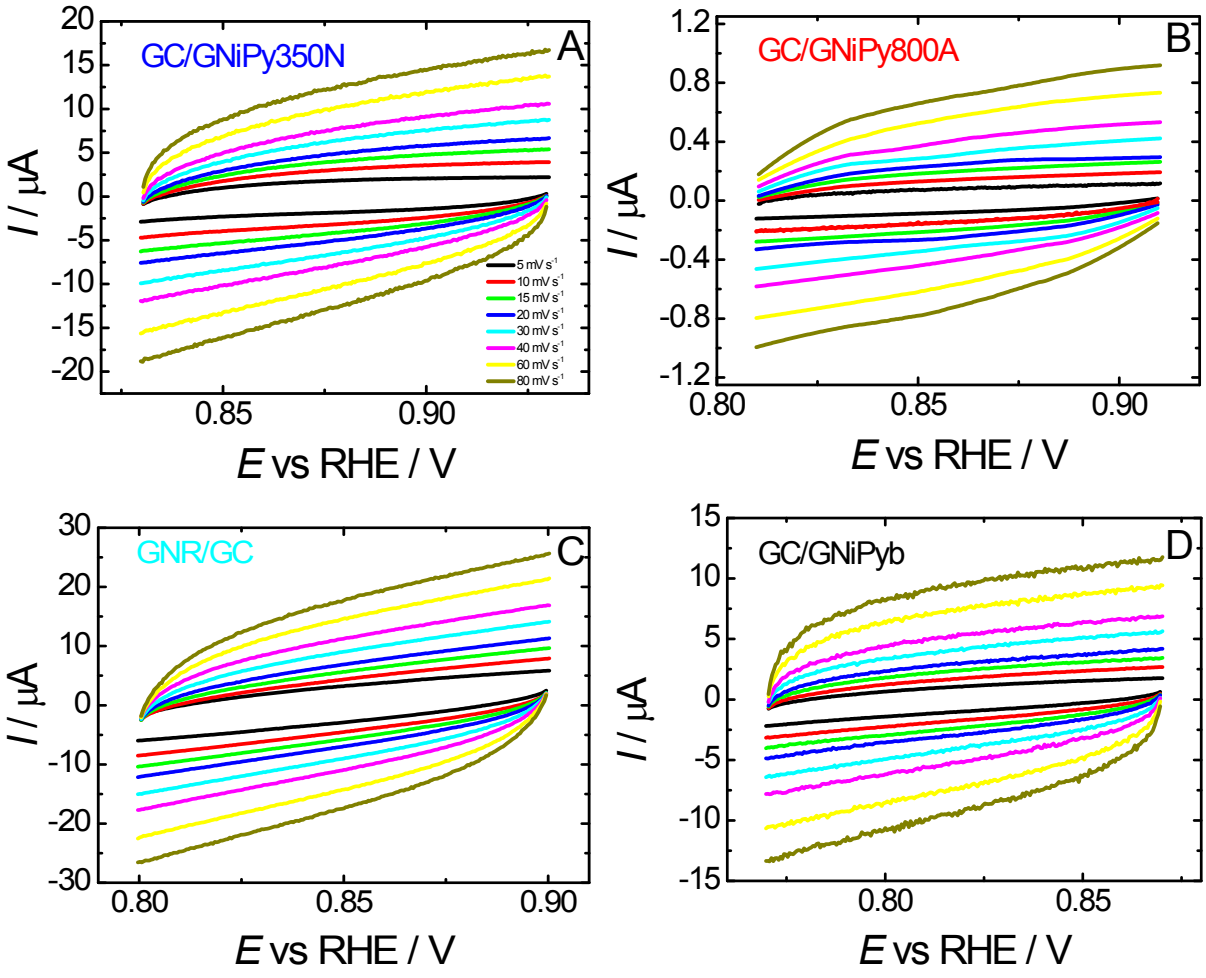

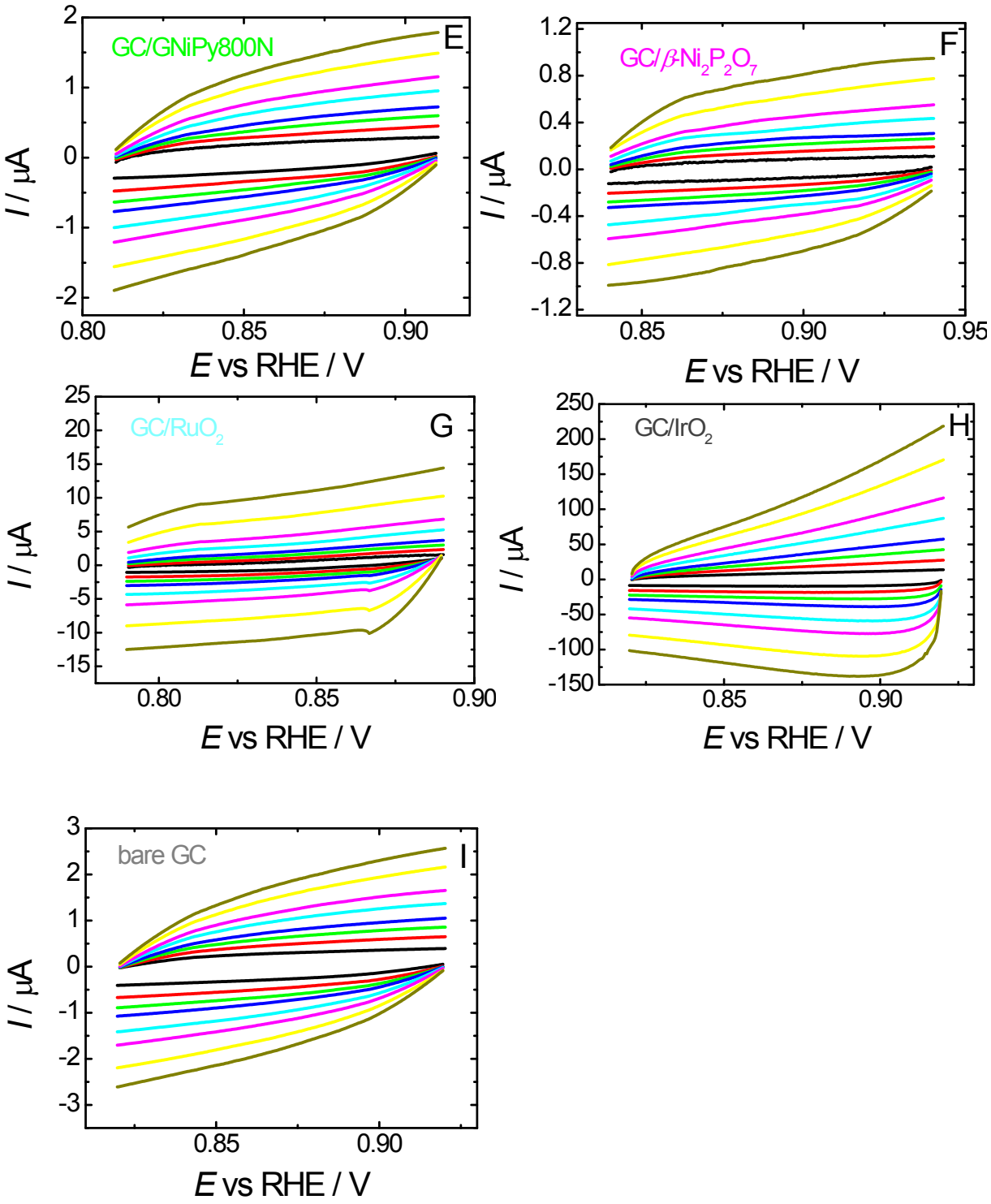

Figure S23. Cyclic voltammograms measured in a non–Faradaic potential region – which also consists of the open circuit potential (OCP) – for modified GC electrodes in N_2–saturated 1M KOH solution after OER. The modified electrodes were kept in each vertex potential for 10 sec before the onset of the next potential sweep. Scans were initiated at higher potentials.

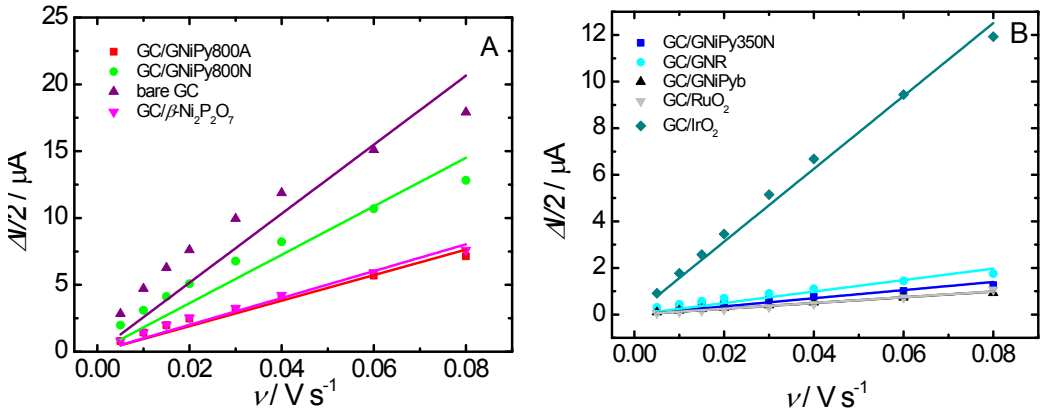

Figure S24. Plots related to differences between the anodic and the cathodic double layer charging currents (Figure S23 after OER) divided by 2 (($\Delta I = I_a - I_c$)/2), measured at the OCP, which is also in a non–Faradaic potential region, relative to the potential scan rates. The slopes of these plots yield the double–layer capacitance (C_{dl}) values (see Table S7) used for determining the ECSA for the modified GC electrodes in N_2–saturated 1 M KOH solution.

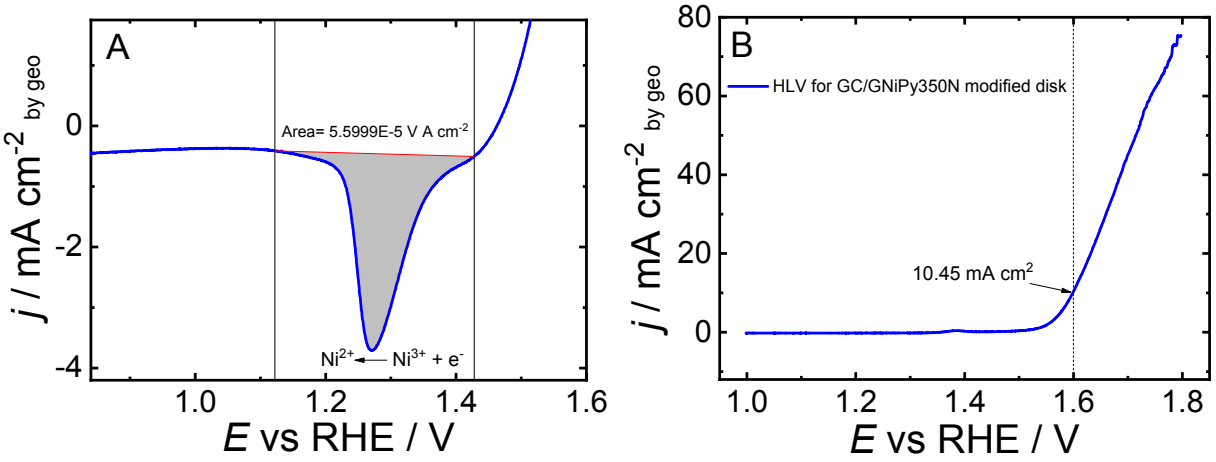

Figure S25. (A) Amplified part of Figure 7A showing the integrated area from the reduction peak used for determining Ni^{2+} surface active species. (B) Hydrodynamic linear potential scan for GC/GNiPy350N modified disk electrode at 5 mV s^{-1} and ω=1600 rpm. Potential scan was initiated at 1.0 V. The Pt ring current density was obtained by maintaining this electrode at 0.4 V while the modified GC disk electrode was scanned in the same solution at ω=1600 rpm. The data were all obtained in N_2–satured 1.0 M KOH solution.

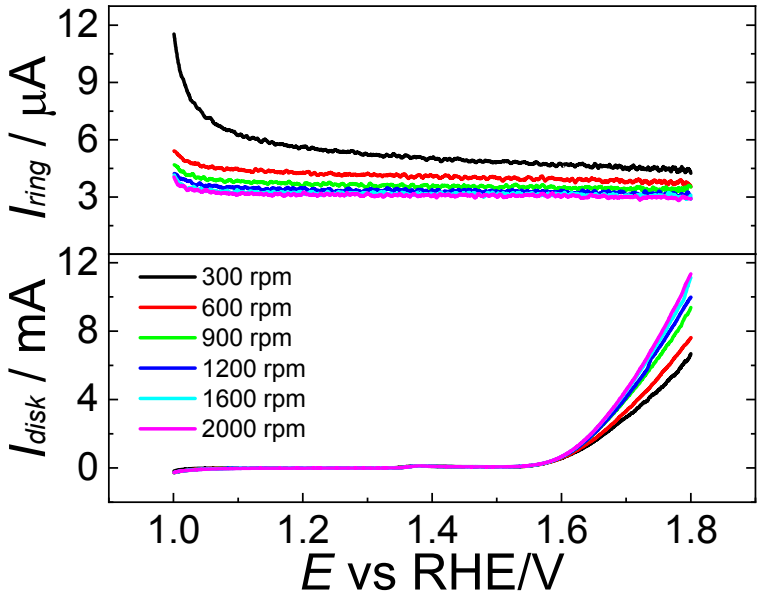

Figure S26. Hydrodynamic linear potential scan (HLS) curves for GC/GNiPy350N disk electrode obtained in N_2–satured 1.0 M KOH solution. Scan rate: 5 mV s^{-1}. Scans were initiated at 1.0 V. The Pt ring current responses were obtained by keeping this electrode at 1.2 V while the modified GC disk electrode was scanned at different ω values.

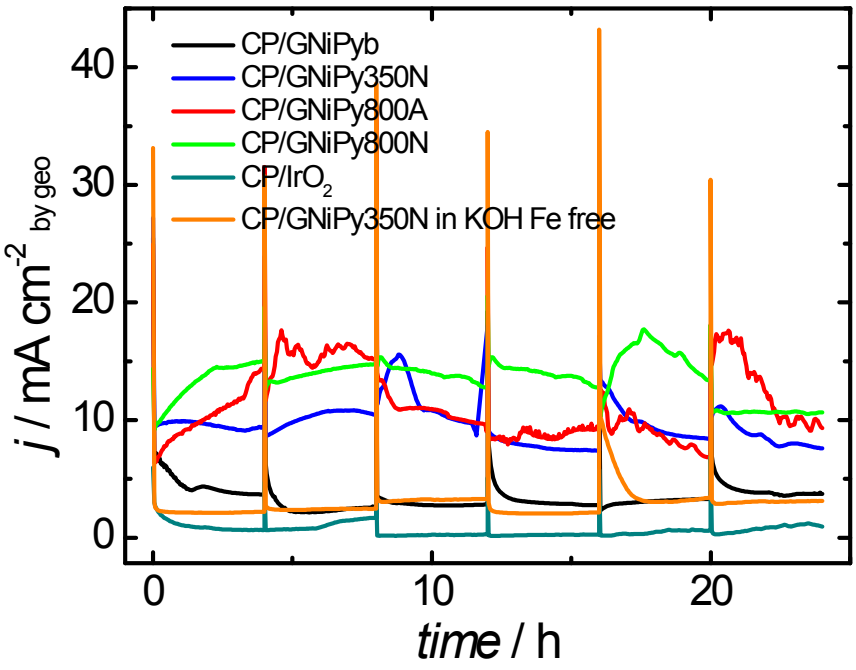

Figure S27. Chronoamperometries for GNiPyb, GNiPy350N, GNiPy800A, GNiPy800N and IrO_2 modified CP electrodes at 1.60, 1.55, 1.62, 1.64, and 1.53 V, respectively, obtained in O_2–saturated 1.0 M KOH solution (potential at which the initial current was 10 mA cm^{-2} by geo) and CP/GNiPy350N electrode at 1.55 V obtained in O_2–saturated purified 1 M KOH solution (Fe free).

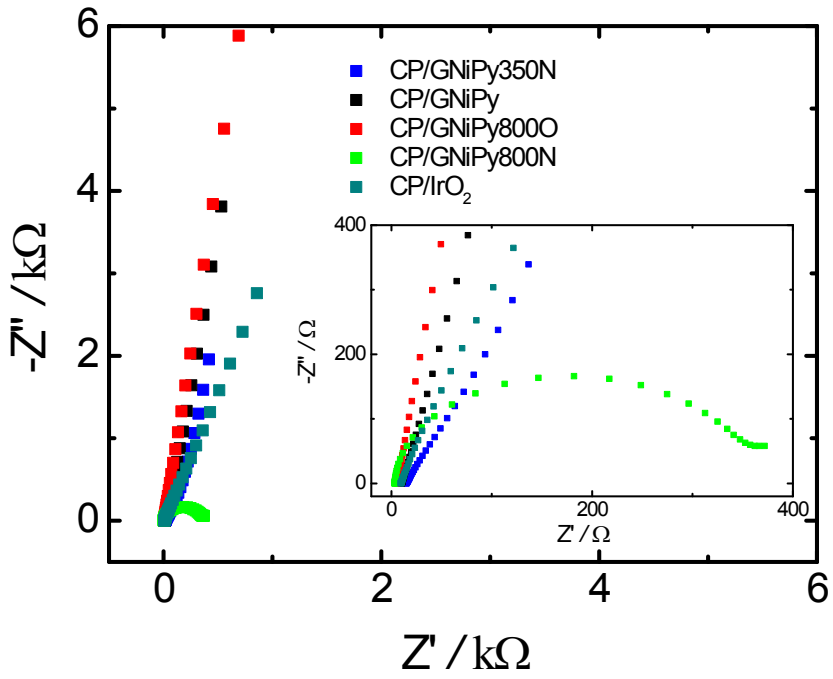

Figure S28. EIS results for bare and modified CP electrodes in N_2–saturated 1 M KOH solution, after OER stability test. Potential perturbation: 10mV (rms). Frequency range: 100kHz – 10 mHz. Constant potential for EIS acquisition: OCP (0.90 V vs. RHE on average).

References

1 L. Trotochaud, S. L. Young, J. K. Ranney, S. W. Boettcher, *J. Am. Chem. Soc.*, 2014, **136**, 6744−6753.

2 D. Kim, J. Kang, B. Yan, K.-D. Seong, Y. Piao, *ACS Sustainable Chem. Eng.*, 2020, **8**, 2843−2853.

3 H. J. Song, H. Yoon, B. Ju, D.-W. Kim, *J Am Ceram Soc*. 2020, **103**, 4748–4753.

4 N. R. Chodankar, I. V. Bagal, S.-W. Ryu, Y.-K. Han, D.-H. Kim, *ChemCatChem* 2019, **11**, 4256–4261.

5 Y. Xiao, S. Deng, M. Li, Q. Zhou, L. Xu, H. Zhang, D. Sun, Y. Tang, *Front. Chem.*, 2019, **7**, 523.

6 S. Surendran, A. Sivanantham, S. Shanmugam, U. Sim, R. K. Selvan, *Sustainable Energy Fuels*, 2019, 3, 2435–2446.

7 S. J. Marje, P. K. Katkar, S. B. Kale, A. C. Lokhande, C. D. Lokhande, U. M. Patil, *J. Alloys Compd.*, 2019, **779**, 49–58.

8 E. Loni, M. H. Siadati, A. Shokuhfar, D. Leybo, D. Kuznetsov, *J. Solid State Chem*, 2020, **290**, 121510.

9 B. Li, R. Zhu, H. Xue, Q. Xu, H. Pang, *J. Colloid Interface Sci.*, 2020, **563**, 328–335.

10 H. J. Song, H. Yoon, B. Ju, D.-Y. Lee, D.-W. Kim, *ACS Catal.*, 2020, **10**, 702−709.

11 D. Liang, C. Lian, Q. Xu, M. Liu, H. Liu, H. Jiang, C. Li, *Appl. Catal. B-Environ.*, 2020, 268, 118417.

12 R. Gond, S. P. V. P. Barpanda, *Chem. Commun.*, 2019, **55**, 11595—11598.
13 J.-T. Ren, G.-G. Yuan, L. Chen, C.-C. Weng, Z.-Y. Yuan, *ACS Sustainable Chem. Eng.*, 2018, **6**, 9793−9803.
14 H. Du, W. Ai, Z. L. Zhao, Y. Chen, X. Xu, C. Zou, L. Wu, L. Su, K. Nan, T. Yu, C. M. Li, *Small*, 2018, **14**, 1801068.
15 J. Wang, H. C. Zeng, *ACS Appl. Mater. Interfaces*, 2018, **10**, 6288−6298.
16 P. Feng, X. Cheng, J. Li, X. Luo, *ChemistrySelect*, 2018, **3**, 760–764.
17 M. Liu, Z. Qu, D. Yin, X. Chen, Y. Zhang, Y. Guo, D. Xiao, *ChemElectroChem*, 2018, **5**, 36–43.